

Optical measurements of pore geometry and fluid velocity in a bed of irregularly packed spheres

Alice Y. L. Huang¹, Michelle Y. F. Huang¹, Hervé Capart², and Rong-Her Chen¹

Abstract

Imaging methods are proposed for the characterisation of liquid flows through transparent porous media of matched refractive index. The methods are based on the analysis of laser-illuminated slices, and specialized for the case in which the porous medium is composed of irregularly packed spheres. They include algorithms for the automated reconstruction of the three-dimensional spheres arrangement based on a laser scan of the packed bed, particle tracking velocimetry applied to the motions of micro-tracers in a laser-illuminated plane, and techniques for the co-registration of geometry and velocity measurements acquired from different slices. The methods are applied to a cylindrical flow cell filled with mono-sized spheres and operated at Reynolds number $Re = 28$. The data produced include the full 3D geometry of the packed spheres assembly, the 2D fluid velocity field in the axial centre-plane of the flow cell, and the corresponding porosity and velocity distributions.

¹ Department of Civil Engineering, National Taiwan University, Taipei 106, Taiwan

² Corresponding Author, Department of Civil Engineering and Hydrotech Research Institute, National Taiwan University, Taipei 106, Taiwan (E-mail: hcapart@yahoo.com).

1 Introduction

Liquid flows through packed beds of spherical particles are of interest for applications such as chemical reactors and separation columns (Hlushkou and Tallarek 2006), and for their role as simplified analogues of flows in natural porous media (Bear 1988). Increasingly, theoretical and empirical efforts are focused on characterizing these flows on the scale of individual pores and the intricate networks that they form. There is therefore a need for measurement techniques that can extract detailed pore-scale geometry and velocimetry data from flow cell experiments. The two main families of techniques suitable for this purpose are tomographic and optical techniques. Tomographic techniques such as Magnetic Resonance Imaging (MRI) and Particle Emission Tomography (PET) rely on specialized apparatus often developed for medical applications to obtain volume images of complex media. An important advantage of these methods is that they do not require transparent materials. Measurements of structure and flow in opaque porous media have been obtained using MRI by Baldwin et al. (1996), Sederman et al. (1997; 1998) Ogawa et al. (2001) and Suekane et al. (2003), and using PET by Khalili et al. (1998). Disadvantages of these techniques include their limited spatial and temporal resolution (for a discussion of the state of the art, see Gladden et al. 2006), susceptibility to certain reconstruction artefacts (Kutsovsky et al. 1996; Chang and Watson 1999), and high equipment costs.

Optical techniques, on the other hand, rely on refractive-index-matched transparent materials (RIM) to gain optical access to the interior of mixed solid-liquid media. This access then allows application of standard flow measurement techniques such as Laser Doppler Anemometry (LDA) and Particle Imaging or Particle Tracking Velocimetry (PIV or PTV). In refractive index-matched porous media, point-wise LDA measurements have been obtained by Johnston et al. (1975) and Yarlagadda and Yoganathan (1989), two-dimensional displacements of advected micro-particles have been acquired by Stephenson and Stewart

(1986), Saleh et al. (1992), Northrup et al. (1993) and Peurrung et al. (1995), while three-dimensional trajectories have been tracked and analysed by Moroni and Cushman (2001). Illuminated slices of porous media, with or without the aid of dyed liquid, have also been used to estimate porosity in transverse cross sections (Stephenson and Stewart, 1986; Peurrung et al. 1995; Rashidi et al. 1996). In the present work, we use optical methods to obtain simultaneous reconstructions of velocities and three-dimensional pore geometry. Both geometry and velocity measurements are extracted from laser-illuminated slices through a liquid-saturated bed of mono-sized spheres. The three-dimensional geometry of the packing is deduced from laser-illuminated halos of the spheres imaged during a vertical scan of the bed. Liquid velocities, on the other hand, are obtained by tracking the motions of laser-illuminated micro-tracers in the axial centre-plane of the flow cell. The resulting two-dimensional velocity field is then put in precise spatial correspondence with the three-dimensional geometry data.

The paper is structured as follows. In section 2, the experimental set-up and conditions are first described. Section 3 then presents the original method developed to reconstruct the three-dimensional arrangement of the spheres based on a laser scan of the porous bed. In section 4, the more conventional approach used to track micro-particles illuminated in a vertical slice of the flow is outlined. The special techniques used to co-register the geometry and velocity data in a common frame of reference are then detailed in section 5. The resulting joint measurements of pore geometry and flow velocity are presented in section 6, before closing with conclusions in section 7.

2 Experimental set-up and conditions

Experiments are conducted in a small darkroom at the Hydrotech Research Institute of National Taiwan University, using the apparatus illustrated in Figs 1 and 2. The flow cell consists of a cylindrical tube having an inner diameter of 5 cm and a height of 40 cm, fed with

liquid from a constant head tank. The tube is encased in an enclosure of square cross section, also filled with liquid, to alleviate light distortion through the curved tube surface. The inside of the tube is filled with a loosely-poured static packing of spheres, all having the same diameter $D = 7$ mm. To avoid trapping air bubbles, the spheres are pluviated into the liquid-filled column and form a random, irregular array constrained by the tube walls. To allow unhindered visual access and light passage through the saturated porous medium, the refractive index-matched materials proposed by Haam et al. (2000) are adopted. The transparent solid spheres are made of polymethyl methacrylate (PMMA), and the fluid used is the liquid para-cymene (benzene, 1-methyl-4-(1-methylethyl)-; Millenium Specialty Chemicals), which has density $\rho = 860 \text{ kg m}^{-3}$ and viscosity $\mu = 1.02 \times 10^{-3} \text{ Pa s}$. The solid and liquid materials share the same index of refraction, with the best transparency obtained at a temperature of around 15°C (Teng 2003).

Digital footage of the flow cell is acquired using an AVT-Marlin F-145B2 charge-coupled device (CCD) camera, operated with a personal computer through the IEEE1394 port. The camera has a resolution of 1392 by 1040 pixels, yielding a pixel size of approx. 0.1 mm for the field of view chosen. It is operated at a frequency $f = 10$ frames per second. To allow both vertical and horizontal slices of the flow to be imaged under the same viewpoint, the camera is oriented at a downwards angle of 45 degrees (Figs 1 and 2). A liquid-filled triangular prism is placed between the camera and the flow cell, and optically coupled to the plane wall of the cell by a liquid layer enclosed by an O-ring. This arrangement allows the inside of the cell to be viewed through a plane window normal to the optical axis of the camera, minimizing optical distortion (Klar et al. 2004).

To permit camera calibration, a frame with marked dots of known 3D positions is placed in the liquid-filled rectangular cavity. Once camera adjustments (orientation, zoom, focus and

aperture) have been frozen, an image of these dots is used to establish the correspondence between the (column, row) pixel coordinates (c,r) and the 3D positions (x,y,z) of points within the viewing volume (Fig. 3). This correspondence is modelled by the ray equation (see Tsorng et al. 2006)

$$\begin{pmatrix} x \\ y \\ z \end{pmatrix} = \mathbf{p} + \lambda \mathbf{q} = \mathbf{p} + \lambda \mathbf{S} \begin{pmatrix} c \\ r \\ 1 \end{pmatrix} \quad (1)$$

where vector \mathbf{p} denotes the 3D position of the projection centre of the perspective, parameter λ codes the position of a 3D point along a ray through \mathbf{p} having direction \mathbf{q} , and where screen matrix \mathbf{S} relates this ray direction to the pixel coordinates (c,r) of the point of interest on the image. This relation can be inverted to yield

$$\begin{pmatrix} \lambda c \\ \lambda r \\ \lambda \end{pmatrix} = \mathbf{A} \begin{pmatrix} x \\ y \\ z \end{pmatrix} + \mathbf{b} \quad (2)$$

where $\mathbf{A} = \mathbf{S}^{-1}$ and $\mathbf{b} = -\mathbf{S}^{-1}\mathbf{p}$. The coefficients of matrix \mathbf{A} and vector \mathbf{b} (as well as parameter λ) intervene linearly in Eq. (2). They can thus be retrieved using least squares from a set of corresponding points of known image and 3D coordinates, as explained in Spinewine et al. (2003). In the present work, 11 calibration marks are used for this purpose. Once the viewpoint has been calibrated, translation from spatial to image coordinates involves two steps: obtain first the left-hand-side vector in Eq. (2), then divide its first and second components by the third.

After the cell and camera have been set up, a laser light sheet is used to illuminate plane slices through the flow cell. The laser used is an Argon Ion laser producing continuous illumination at a power of approximately 250 mW. An optical fibre conveys the laser beam to a headpiece where a cylindrical lens spreads the beam into a light sheet having a thickness of

approximately 0.5 mm. In order to acquire both geometric and velocimetric data, the light sheet is used in two different ways (Fig. 3). To construct a volumetric image of the packed bed of spheres, the headpiece is first mounted on a screw-driven railed carriage. The laser sheet translates vertically at constant speed, illuminating as it travels successive transverse cross sections of the porous column (Fig. 3a). To obtain velocimetric data, on the other hand, the laser sheet is mounted on a static tripod and used to illuminate the axial centre-plane of the flow cell (Fig. 3b). Fluid motions are made visible by seeding the liquid with tracer micro-particles (Polyamide Seeding Particles; Dantec Dynamics; diameter 50 μm , density 1.03 kg m^{-3}). These micro-particles are introduced in the constant head tank, where mixing is enhanced by an agitator.

For the velocity measurements, steady downwards flow is induced under constant head conditions, and the flow rate is measured by collecting the discharge at the outlet. For the experiments reported below, the flow rate through the column was $Q = 4.60 \text{ ml s}^{-1}$, corresponding to a Reynolds number $\text{Re} = 28$, with the Reynolds number defined by

$$\text{Re} = \frac{\rho D Q}{\mu A \varepsilon}, \quad (3)$$

where D is the diameter of the spheres, A is the cross-sectional area of the flow cell, and $\varepsilon = 0.48$ is the porosity of the granular assembly. This places the flow in the viscous-inertial regime (see Hlushkou and Tallarek 2006), a steady laminar flow regime intermediate between creeping flow (for which fluid inertia can be neglected) and turbulent flow (for which the fluid motions become unsteady at the pore scale).

3 Three-dimensional geometry scan

As the laser light sheet traverses the liquid-saturated bed of spheres, light diffraction occurs at the intersections between the laser plane and the surfaces of the spheres. Bright circular halos

are therefore generated in the laser plane, with halos taking variable diameters depending on the relative position of the spheres. Such halos were recently used by Hsu and Capart (2007) to track the motions of immersed spheres. In the present work, the halos are observed under an oblique angle and adopt elliptical shapes on the raw digital footage (Fig. 4a). We exploit these halos as follows to reconstruct the three-dimensional arrangement of the irregularly packed spheres. For the geometry measurements, the laser light sheet is given a horizontal orientation and scanned vertically at the constant speed $W = 2.5 \text{ mm s}^{-1}$. Each frame k of the corresponding image sequence is then associated with the horizontal plane

$$z = z_k = z_0 + kh, \quad (4)$$

where $h = W/f = 0.25 \text{ mm}$ is the displacement between successive slices. Defining

$$x_i = x_0 + ih, \quad y_j = y_0 + jh, \quad (5,6)$$

a volumetric image $J(i, j, k)$ composed of cubic voxels of side h is constructed by stacking together transformed images $J_k(i, j)$ obtained by rectifying the raw frames $I_k(c, r)$. The position of each point (x_i, y_j) of the slice is first converted to image coordinates (c_{ij}, r_{ij}) using Eq. (2):

$$\begin{pmatrix} \lambda_{ij} c_{ij} \\ \lambda_{ij} r_{ij} \\ \lambda_{ij} \end{pmatrix} = \mathbf{A} \begin{pmatrix} x_i \\ y_j \\ z_k \end{pmatrix} + \mathbf{b}. \quad (7)$$

The transformed image $J_k(i, j)$ is then obtained by sampling the original image $I_k(c, r)$ at sites (c_{ij}, r_{ij}) by bilinear interpolation. In practice, this procedure must be modified slightly to alleviate optical distortion and retrieve an upright flow cell. This is done by adding a quadratic correction term to Eq. (5):

$$x_i = x_0 + ih + \alpha z_k^2 + \beta z_k + \gamma. \quad (8)$$

The resulting volumetric image $J(i, j, k)$ is composed of a stack of ortho-rectified slices in which the laser-illuminated elliptical halos of the spheres are deformed back to their circular

shapes (Fig. 4b). Upon stacking these pixel rings on top of one another, each sphere is imaged as a spherical shell of bright voxels, where all shells have the same diameter D .

The procedure used to identify spheres in the three-dimensional voxel image can be more easily explained by considering first the analogue two-dimensional case illustrated in Fig. 5, in which spheres of uniform size are modelled by circles of constant diameter. Assume then a 2D image $J(i, j)$ defined on grid (x_i, y_j) and featuring irregularly positioned circles of diameter D imaged as rings of bright pixels (Fig. 5a). To identify these circles, a discrete filter approximating a ring of diameter D is scanned over the whole image, yielding convolution peaks where the centre of the filter coincides with the centre of a circle. To construct the filter, we represent a circle of diameter D centred at $(0,0)$ as the zero level set of function

$$\phi(x, y) = x^2 + y^2 - (D/2)^2, \quad (9)$$

and sample this function on grid (x_m, y_n) to obtain the array $\phi_{m,n} = \phi(x_m, y_n)$. We then use the discrete delta function approach of Smereka (2006) to construct the discrete filter

$$F(m, n) = \delta^{(+x)}(m, n) + \delta^{(-x)}(m, n) + \delta^{(+y)}(m, n) + \delta^{(-y)}(m, n), \quad (10)$$

where $\delta^{(+x)}(m, n) = \begin{cases} |\phi_{m+1,n}(\phi_{m+1,n} - \phi_{m-1,n})| & \text{if } \phi_{m,n}\phi_{m+1,n} \leq 0, \\ h |\phi_{m+1,n} - \phi_{m,n}| \|\nabla^\varepsilon \phi_{m,n}\| & \\ 0, & \text{otherwise,} \end{cases}$ (11)

$$\delta^{(-x)}(m, n) = \begin{cases} |\phi_{m-1,n}(\phi_{m+1,n} - \phi_{m-1,n})| & \text{if } \phi_{m,n}\phi_{m-1,n} < 0, \\ h |\phi_{m,n} - \phi_{m-1,n}| \|\nabla^\varepsilon \phi_{m,n}\| & \\ 0, & \text{otherwise,} \end{cases}$$
 (12)

and likewise for the other components. In the above expressions,

$$|\nabla^\varepsilon \phi_{m,n}| = \frac{1}{h} \sqrt{(\phi_{m+1,n} - \phi_{m-1,n})^2 + (\phi_{m,n+1} - \phi_{m,n-1})^2 + \varepsilon}, \quad (13)$$

where ε is a small number introduced to avoid division by zero. The resulting filter $F(m, n)$, illustrated in Fig. 5b, models a ring of pixels of well-balanced illumination. We now convolute the image $J(i, j)$ with filter $F(m, n)$ to obtain a transformed image

$$K(i, j) = \sum_m \sum_n J(i - m, j - n) F(m, n). \quad (14)$$

The convolution response is the strongest at the centres of the circles, where localized illumination peaks are obtained in the transformed image (Fig. 5c). The peak locations can finally be retrieved to sub-pixel accuracy using standard methods (see e.g. Capart et al. 2002), yielding the desired set of centres and circles (Fig. 5d). Although the notations become more complicated, the above method is straightforward to generalize to three dimensions. As illustrated in Fig. 6a, the objective is to identify shells of bright pixels in the laser-scanned volumetric image of the porous column $J(i, j, k)$. Convolution with a three-dimensional version of the discrete filter of Eq. (10) yields the transformed volumetric image illustrated in Fig. 6b, where illumination peaks indicate sphere centres. To obtain this stack of 300 convoluted slices shown, 336 rectified video frames were used. As in the two-dimensional case, the locations of the peaks can then be identified and refined to sub-pixel accuracy. The spheres of positions (X, Y, Z) extracted in this fashion from the three-dimensional laser scan are illustrated in Fig. 6c. The method above is specialized for the identification of mono-sized spheres in volumetric images of their laser-illuminated shells. A more general method applicable to spheres of arbitrary size is the Hough transform approach described in Cao et al. (2006).

4 Micro-particle velocities

Upon seeding the liquid with micro-particles, the flow is imaged in the laser-illuminated vertical centre-plane. Various methods are available to extract velocity measurements from images of moving micro-particles. For refractive-index-matched flows, both particle tracking velocimetry (PTV; e.g. Moroni and Cushman 2001) and particle image velocimetry (PIV; e.g. Zachos et al. 1996) have been used by previous researchers. Unfortunately, these automated techniques are subject to requirements which are not met by our footage. Unsupervised PTV

relies on minimum displacement, path regularity, or pattern coherence to establish particle correspondences between frames (see e.g. Capart et al. 2002). The interrogation windows used by PIV methods, on the other hand, must include a sufficient number of particle images, which cannot undergo excessive shear (Huang et al. 1993). Complicating features in the present experiments include irregular pore space, steep gradients and changes of directions, and particles moving in and out of the laser light sheet. Furthermore, the temporal and spatial resolution of our camera did not permit us to compensate for these difficulties by reducing inter-frame displacements or increasing the seeding density. A supervised, semi-manual particle tracking procedure was therefore adopted.

To facilitate visual inspection, colorized images are assembled in the following way (see Fig. 7a). After subtraction of the averaged background, multiple exposures are assembled from four successive frames using a blue-red-green-blue coding scheme. Let $R(m,n)$, $G(m,n)$ and $B(m,n)$ denote the RGB layers of the colorized image. To retrieve displacements from frame k to frame $k+1$, these layers are set to

$$R(m,n) = I_k(m,n), \quad G(m,n) = I_{k+1}(m,n), \quad (15,16)$$

$$B(m,n) = \max(I_{k-1}(m,n), I_{k+2}(m,n)), \quad (17)$$

where $I_k(m,n)$ is the k -th frame of the monochrome video sequence. Red and green particles can be identified at (column, row) pixel coordinates $(c_i^{(k)}, r_i^{(k)})$ and $(c_j^{(k+1)}, r_j^{(k+1)})$, respectively. Particle tracking then amounts to establishing the matching $j(i)$ between red and green particles most likely to correspond to one and the same physical particle. This is done using manual mouse clicks, aided by the visual clues provided by the blue-red-green-blue alignments, sizes and illumination intensities of the micro-particles. Pairings are recorded only when they can be ascertained with a sufficient degree of confidence. Illustrated in Fig. 7b, the procedure was checked to yield consistent results when performed by different operators.

To capture particles that are moving more slowly, the procedure is repeated using frames $\{k-2, k, k+2, k+4\}$ instead of $\{k-1, k, k+1, k+2\}$. Overall, 40 colorized multiple exposures were used to obtain a total of 3757 individual velocity vectors. Manual mouse-clicks are also used to retrieve points along the elliptical intersections between the laser plane and the sphere boundaries. The pixel coordinates (c, r) of micro-particle positions and contour points are then transformed to spatial (y, z) coordinates by seeking intersections of rays $\mathbf{x}(\lambda) = \mathbf{p} + \lambda \mathbf{q}$ with vertical centre-plane $x = 0$. Parameter λ is first determined from linear equation

$$x = p_1 + \lambda(S_{11}c + S_{12}r + S_{13}) = 0, \quad (18)$$

where p_α and $S_{\alpha\beta}$ are the components of vector \mathbf{p} and matrix \mathbf{S} in Eq. (1). The remaining two lines of this linear system are then used to retrieve coordinates y and z of point $\mathbf{x} = (x, y, z)$. After transformation, circles are fitted by least squares to the contour points. Velocity vectors in the plane are estimated from

$$v_i^{(k+1/2)} = \frac{y_{j(i)}^{(k+1)} - y_i^{(k)}}{\Delta t}, \quad w_i^{(k+1/2)} = \frac{z_{j(i)}^{(k+1)} - z_i^{(k)}}{\Delta t}, \quad (19, 20)$$

where $\Delta t = 1/f$, and where v, w are the velocity components in the y, z directions. These vectors are assigned to the midpoint positions

$$y_i^{(k+1/2)} = \frac{1}{2}(y_i^{(k)} + y_{j(i)}^{(k+1)}), \quad z_i^{(k+1/2)} = \frac{1}{2}(z_i^{(k)} + z_{j(i)}^{(k+1)}). \quad (21, 22)$$

Results from this procedure are shown in Fig. 7c. Under the assumption of steady flow, raw velocity vectors obtained at different times $t_{k+1/2}$ can finally be pooled together into a single two-dimensional velocity field (v, w) . Prior to statistical analysis, raw velocity vectors are binned into small square cells of dimensions $\Delta y = \Delta z = 1$ mm, averaging together vectors falling within the same cell. Velocity profiles and distributions are then constructed from the resulting cell averages (see section 6). This is needed to counter the possible sampling bias associated with the semi-manual tracking procedure, which could select higher numbers of vectors in certain zones. It is also possible to gauge errors on individual velocity vectors by

looking at differences Δv , Δw between the raw velocity vectors and those interpolated from the binning grid at raw vector positions. The resulting error estimates are

$$\varepsilon_v = \frac{(\Delta v)_{75} - (\Delta v)_{25}}{2} = 0.6 \text{ mm/s}, \quad \varepsilon_w = \frac{(\Delta w)_{75} - (\Delta w)_{25}}{2} = 1.0 \text{ mm/s}, \quad (23, 24)$$

where indices 25 and 75 denote the first and third quartile of the corresponding distributions. Compared to the velocity range of approx. 2 cm/s, this amounts to relative errors of 3 to 5 %. As a second check on the accuracy of the velocity measurements, the overall mean axial velocity (averaged over the binning grid) $|\bar{w}| = 0.491$ cm/s can be used to estimate the liquid discharge through the cell. The resulting estimate $Q = |\bar{w}| \cdot \varepsilon A = 4.63$ ml/s is within 1 % of the value $Q = 4.60$ ml/s measured at the outlet of the flow cell.

5 Co-registration of velocity and geometry data

Because of imperfect light sheet alignment and perspective distortion due to refractive effects, the velocimetry plane is not yet in precise spatial correspondence with the geometry scan. A correction procedure is therefore needed to adjust the two sets of spatial data with each other. This spatial co-registration problem is commonly encountered in medical imaging applications when seeking to fuse measurements from different sensors. In the present work, the following two-step procedure is adopted: first, a 3D translation and rotation adjustment of the velocimetry plane is made to bring its circular halos in closer correspondence with the scanned sphere array; secondly, in-plane deformations are applied to make halo centres coincide. The first step is performed using a variant of the Iterative Closest Point (ICP) procedure widely used in machine vision (Besl and McKay 1992). On the one hand, let (y_i, z_i) and d_i denote the centre positions and diameters of the circular halos identified in the velocimetry plane $x = 0$. The apparent diameter provides a measure of the sphere offset relative to the plane, but it is unclear whether this offset is positive or negative. The corresponding sphere positions relative to the plane are thus known except for the ambiguity

of their relative placement to the front or back of the plane (see Fig. 8a). Possible sphere positions are given by

$$\mathbf{x}_i^{(-)} = \left(-\frac{1}{2}\sqrt{D^2 - d_i^2}, y_i, z_i \right) \quad \text{or} \quad \mathbf{x}_i^{(+)} = \left(+\frac{1}{2}\sqrt{D^2 - d_i^2}, y_i, z_i \right), \quad (25)$$

where the true relative sphere position belongs to either one of the two sets. On the other hand, let $\mathbf{X}_j = (X_j, Y_j, Z_j)$ denote the full set of sphere positions extracted from the geometry scan. A pairing $j(i)$ between the two sets of spheres can be established by finding which of the candidate sphere positions $\mathbf{x}_i^{(-)}$ and $\mathbf{x}_i^{(+)}$ lie closest to which sphere positions \mathbf{X}_j . The pairing is given by

$$j(i) = \underset{j}{\operatorname{argmin}} \{ \min(\| \mathbf{X}_j - \mathbf{x}_i^{(-)} \|, \| \mathbf{X}_j - \mathbf{x}_i^{(+)} \|) \} \quad (26)$$

where $\operatorname{argmin}\{g(j)\}$ returns the argument j which minimizes function $g(j)$. The most likely sphere position \mathbf{x}_i relative to the plane is further given by

$$\begin{cases} \mathbf{x}_i = \mathbf{x}_i^{(-)}, & \text{if } \| \mathbf{X}_{j(i)} - \mathbf{x}_i^{(-)} \| \leq \| \mathbf{X}_{j(i)} - \mathbf{x}_i^{(+)} \|, \\ \mathbf{x}_i = \mathbf{x}_i^{(+)}, & \text{otherwise.} \end{cases} \quad (27)$$

Once this correspondence between spheres \mathbf{x}_i and $\mathbf{X}_{j(i)}$ of the two sets is established, the quaternion-based algorithm of Horn (1987) is used to determine the translation vector \mathbf{t} and rotation matrix \mathbf{R} that will bring transformed positions \mathbf{x}'_i closest (in the least squares sense) to positions $\mathbf{X}_{j(i)}$, where

$$\mathbf{x}'_i = \begin{pmatrix} x'_i \\ y'_i \\ z'_i \end{pmatrix} = \mathbf{t} + \mathbf{R} \begin{pmatrix} x_i \\ y_i \\ z_i \end{pmatrix}. \quad (28)$$

The matching operation of Eq. (26) can then be performed again on the basis of the transformed positions \mathbf{x}'_i , and the procedure iterated until convergence, following the Iterative Closest Point algorithm (ICP) of Besl and McKay (1992). In the present case, the initial mismatch (Fig. 8b) is relatively small, and 2 to 3 iterations are sufficient. The halo correspondences after optimal translation and rotation are illustrated in Figs 8c and 8d,

respectively. Substantial improvement is obtained compared to the non-adjusted halos (Fig. 8b), but the fit is not yet perfect. A second adjustment step is therefore needed, for which in-plane deformations are applied to the velocimetry plane data. After optimal translation and rotation, the 3D position of a point having original position $\mathbf{x} = (0, y, z)$ in the velocimetry plane becomes

$$\mathbf{x}' = \mathbf{t} + y\mathbf{R}^{(2)} + z\mathbf{R}^{(3)} \quad (29)$$

where $\mathbf{R}^{(2)}$ and $\mathbf{R}^{(3)}$ have unit lengths and represent the mutually orthogonal second and third column vectors of rotation matrix \mathbf{R} . To perform the in-plane deformation, it is convenient to project the scanned 3D positions of the spheres onto the same plane to obtain

$$\mathbf{X}'_j = \mathbf{t} + \eta_j \mathbf{R}^{(2)} + \zeta_j \mathbf{R}^{(3)}, \quad (30)$$

where the projected coordinates of the centres of the spheres (η_j, ζ_j) are given by

$$\eta_j = (\mathbf{X}_j - \mathbf{t}) \cdot \mathbf{R}^{(2)}, \quad \zeta_j = (\mathbf{X}_j - \mathbf{t}) \cdot \mathbf{R}^{(3)}. \quad (31)$$

A deformation field $(\sigma(y, z), \tau(y, z))$ can then be defined which brings the circle centres and projected sphere centres in perfect spatial correspondence with each other, i.e.

$$\sigma(y_i, z_i) = \eta_{j(i)} - y_i \quad \text{and} \quad \tau(y_i, z_i) = \zeta_{j(i)} - z_i. \quad (32,33)$$

This deformation field can be extended to the whole plane by Delaunay interpolation, after mirror reflection about the left and right tube boundaries to deal with near-wall zones. One can therefore obtain translated, rotated, and deformed coordinates of any point in the velocimetry plane using

$$\mathbf{x}'' = \mathbf{t} + (y + \sigma(y, z))\mathbf{R}^{(2)} + (z + \tau(y, z))\mathbf{R}^{(3)}. \quad (34)$$

In particular, the transformation can be applied to the successive positions of the laser-illuminated micro-tracers, yielding a transformed velocity field that is precisely co-registered with the 3D sphere positions of the geometry scan.

6 Results and discussion

Figures 9 to 12 present the measurement results. Results for the packing geometry of the spheres are first shown in Fig. 9. Panel 9b shows the porosity distribution obtained by averaging a sequence of horizontal cross-sections through the reconstructed sphere arrangement of Fig. 6c. For qualitative comparison, an oblique long exposure view constructed from 50 frames of the geometry scan is shown in Fig. 9a. The porosity distribution exhibits a clear annular structure, with spheres located preferentially within concentric rings. Rings are most distinct near the outer perimeter, and gradually lose their coherence towards the central axis of the tube. To a lesser degree, some granularity can also be observed within each ring, reflecting the internal organization of the spheres within each annulus.

Figure 10 shows the co-registered fluid velocities and packing geometry in the axial plane, along with a long exposure view constructed from the video footage. Panels 10a and 10c show this laser-illuminated long exposure, constructed by registering at each pixel the maximum illumination experienced during a sequence of frames. In panels 10b and 10d, the circular contours represent the intersections between the velocimetry plane and the three-dimensional packing of spheres reconstructed from the geometry scan. The vectors, on the other hand, represent the velocity field deduced from micro-particle displacements, after adjustment to the geometry data using the co-registration procedure of the previous section. Panels 10a and 10b present an overview of the flow cell axial plane, while panels 10c and 10d zoom in on a local window. In Fig. 10, the irregular positions and diameters of the sphere halos reflect the constrained random arrangement of the spheres within the flow cell. During the reconstruction procedure, spheres were not constrained to avoid inter-penetrating each other. As seen in Fig. 10, the results nevertheless satisfy this rigidity constraint (spheres overlap at certain points of contact by at most 0.7 mm), providing some confidence in the

reliability of the method.

The local pattern adopted by the porous flow through the irregular pore space is shown in close-up in Fig. 10d. The complicated flow pattern features a set of stagnation points along the upper portions of the spheres (facing the mean downwards current), where the flow bifurcates left and right into different threads. In the wakes of the spheres, localized zones of separation are observed, with certain recognizable whirls of vorticity. At this Reynolds number $Re = 28$, the flow pattern around individual spheres is not symmetric in the upstream-downstream direction, reflecting the influence of liquid inertia. Nevertheless, vectors acquired at different times during the video sequence align into coherent streamlines, illustrating the steady nature of the flow. The close-up also exhibits a good correspondence between the flow pattern and the sphere boundaries, indicating that the spatial co-registration procedure was successful. The data produced can thus be exploited to validate direct numerical simulations of the porous flow, with the full 3D geometry of the packed bed provided as input.

Transverse profiles across the flow cell are plotted in Fig. 11. Figure 11a shows the radial profile of porosity obtained by averaging the porosity map of Fig. 9b along concentric annuli. As observed previously by Mueller (1997) and Spinewine et al. (2003), spheres tend to organize into layers in the vicinity of solid boundaries, leading to a set of regularly spaced porosity troughs (solid fraction peaks), with the spacing corresponding approximately to the particle diameter $D = 0.7$ cm. The peaks and troughs are sharpest next to the tube wall, and become gradually less sharp as one moves inward. Figure 11b shows the corresponding transverse profile of axial velocity, averaged over vertical slices of the plane velocity field. Like the porosity profile, the velocity profile exhibits a series of peaks and troughs. These peaks and troughs are not perfectly aligned with those of the porosity profile, partly because

the velocity is averaged from a single axial plane, whereas the porosity is averaged from fully three-dimensional data. Nevertheless, the velocity and porosity profiles are roughly in phase with each other indicating that, on average, the liquid tends to flow faster where the porosity is higher. Similar relationships between porosity and axial velocity have been observed previously in both computations (Magnico 2003) and experiments (Ren et al. 2005).

Statistical distributions of the transverse and axial velocity components are presented in Fig. 12. They were obtained by distributing the gridded velocity measurements into non-overlapping bins of width 1 mm/s, and counting the resulting frequencies. The corresponding histograms are presented in physical units in panels 12a and 12b. To facilitate comparison with results by other researchers, distributions are plotted in normalized forms in panels 12c and 12d. Figure 12c normalizes the distribution of transverse velocity by its standard deviation. For this component of the velocity field, the distribution is highly symmetric around a mean close to zero, and is reasonably well approximated by a Gaussian normal distribution. As in the measurements by Moroni and Cushman (2001, not shown) the Gaussian profile nevertheless slightly underestimates the central peak of the transverse velocity data. Figure 12d shows the distribution of axial velocity normalized by its mean value. In this normalized form, our measurements for Reynolds number $Re = 28$ (black dots) can be compared with the data of Moroni and Cushman (2001) obtained at lower Reynolds numbers in the range $Re = 0.05$ to 0.13 (open symbols). In this relatively narrow Reynolds number range, Moroni and Cushman noted a high degree of similarity between normalized axial velocity distributions. We find in the present study that this similarity is preserved up to the higher Reynolds number $Re = 28$. Although this Reynolds number already lies in the viscous-inertial regime, our velocity distribution closely matches the distributions obtained by Moroni and Cushman (2001) for creeping flow.

Axial velocity distributions in porous media flow have been obtained in various earlier studies, from both Nuclear Magnetic Resonance (NMR) experiments (e.g. Kutsovsky et al. 1996; Lebon et al. 1996) and hydrodynamic computations (e.g. Maier et al. 1998; Magnico 2003). The shapes of the corresponding curves differ from the shapes obtained by particle tracking velocimetry (PTV) in our work and that of Moroni and Cushman (2001). In particular, they tend to feature sharp peaks at velocities near zero, whereas the PTV results (see Fig. 12d) exhibit smoother peaks located to the right of the origin. This may be because PTV results do not sample liquid velocities in certain low velocity regions like the immediate neighbourhood of the sphere surfaces. Moroni and Cushman filter out the tracer bubbles which have deposited on the sphere surfaces, and we likewise filter out micro-particles close to the sphere halos or sedimented on the sphere surfaces by subtracting background images prior to particle tracking. Moreover, low velocity dead zones of the flow may fail to be reached by tracer particles injected into the cell (see Fig. 10). As a result, velocities near zero may be under-sampled in comparison with NMR and computational data. Alternatively, velocities near zero may be over-sampled by NMR, due to partial volume effects associated with voxels that are only partly occupied by liquid along solid particle boundaries (Tang et al. 1993; Elkins and Alley 2007).

7 Conclusions

In this paper, methods for the analysis of pore-scale flows in packed beds of spheres were presented, relying on the imaging of laser-illuminated slices through a refractive-index-matched flow cell. The methods include automated techniques for the reconstruction of the three-dimensional sphere arrangement, and methods to bring plane velocimetry data in precise spatial correspondence with the arrayed spheres. Applied to a cylindrical cell filled with loose-poured spheres and subject to a downwards liquid flow, the methods were used to obtain a variety of data. A map of the average porosity distribution over

the tube cross section was derived from the geometrical scan, and used to highlight the annular structure of the bed of packed spheres. Comparison of transverse porosity and axial velocity profiles show that the fluid tends to flow faster in the high porosity bands located between rings of spheres. In the axial centre plane, a detailed view of the liquid flow field and its relationship with the boundaries of the spherical particles was obtained. Some upstream-downstream asymmetry of the flow around individual spheres was interpreted to reflect the influence of fluid inertia. Nevertheless, comparison of velocity distribution results with the data of Moroni and Cushman (2001) obtained at lower Reynolds numbers suggests that normalized distributions remain highly similar in shape at least up to the Reynolds number $Re = 28$ attained in the present experiments. Distribution shapes obtained by particle tracking velocimetry, however, differ from those obtained in nuclear magnetic resonance experiments and hydrodynamic calculations. Because the data produced in the present experiments include the full 3D geometry of the porous medium as well as co-registered 2D velocities, they are suitable for comparison with direct numerical simulations of the flow, and for statistical analysis of structure-flow correlations. Since they may help resolve discrepancies between approaches, and shed further light on the dynamics of liquid flow of porous media, these two avenues are considered for further work.

Acknowledgments

Support for this research was provided by the National Science Council of Taiwan. The assistance of Tai-An Chi and Jason C.C. Su (National Taiwan University, Taiwan), for the laboratory experiments and for the implementation of the co-registration algorithms, and Damien Douxchamps (Nara Institute of Science and Technology, Japan), for imaging ideas and IEEE1394 camera tips, is also gratefully acknowledged.

References

- Baldwin CA; Sederman A J; Mantle MD; Alexander P; Gladden LF** (1996) Determination and characterization of the structure of a pore space from 3D volume images. *J Colloid Interface Sci* 181: 79–92
- Bear J** (1988) Dynamics of Fluids in Porous Media. Dover Publications, New York
- Besl PJ; McKay ND** (1992) A method for registration of 3D shapes. *IEEE Trans Patt Anal Machine Intell* 14: 239–256
- Cao MY; Ye CH; Doessel O; Liu C** (2006) Spherical parameter detection based on hierarchical Hough transform. *Pattern Recog Lett* 27: 980–986
- Capart H; Young DL; Zech Y** (2002) Voronoï imaging methods for the measurement of granular flows. *Exp Fluids* 32: 121–135
- Chang CTP; Watson AT** (1999) NMR imaging of flow velocity in porous media. *AIChE Journal* 45: 437–444
- Elkins CJ; Alley MT** (2007) Magnetic resonance velocimetry: applications of magnetic resonance imaging in the measurement of fluid motion. *Exp Fluids* 43: 823–858
- Gladden LF; Akpa BS; Anadon LD; Heras JJ; Holland DJ; Mantle MD; Matthews S; Mueller C; Sains MC; Sederman AJ** (2006) Dynamic MR imaging of single- and two-phase flows. *Chem Eng Res Design* 84: 272–281
- Haam SJ; Brodkey RS; Fort I; Klaboch L; Placnik M; Vanecek V** (2000) Laser Doppler anemometry measurements in an index of refraction matched column in the presence of dispersed beads – Part I. *Int J Multiphase Flow* 26: 1401–1418
- Hlushkou D; Tallarek U** (2006) Transition from creeping via viscous-inertial to turbulent flow in fixed beds. *J Chromatogr A* 1126: 70–85
- Horn BKP** (1987) Closed-form solution of absolute orientation using unit quaternions. *J Opt Soc Amer A* 4: 629–642
- Hsu HC; Capart H** (2007) Enhanced upswing in immersed collisions of tethered spheres.

Phys Fluids 19, art. 101701: 1–4

Huang HT; Fiedler HE; Wang JJ (1993) Limitation and improvement of PIV. Part I: Limitation of conventional techniques due to deformation of particle image patterns. *Exp Fluids* 15: 168–174

Johnston W; Dybbs A; Edwards R (1975) Measurement of fluid velocity inside porous media with a laser anemometer. *Phys Fluids* 18: 913–914

Khalili A; Basu AJ; Pietrzyk U (1998) Flow visualization in porous media via Positron Emission Tomography. *Phys Fluids* 10: 1031–1033

Klar M; Jehle M; Jähne B; Detert M; Jirka GH; Köhler HJ; Wenka T (2004) Simultaneous 3-D PTV and micro-pressure sensor equipment for flow analysis in a subsurface gravel layer. Proc. 2nd Int. Conf. on Fluvial Hydraulics (M. Greco, A. Caravetta, and R. Della Morte, Eds.), Napoli, Italy (June 2004), pp. 703–712

Kutsovsky YE; Scriven LE; Davis HT; Hammer BE (1996) NMR imaging of velocity profiles and velocity distributions in bead packs. *Phys Fluids* 8: 863–871

Lebon L; Oger L; Leblond J; Hulin JP; Martys NS; Schwartz LM (1996) Pulsed gradient NMR measurements and numerical simulation of flow velocity distribution in sphere packings. *Phys Fluids* 8: 293–301

Magnico P (2003) Hydrodynamic and transport properties of packed beds in small tube-to-sphere diameter ratio: pore scale simulation using an Eulerian and a Lagrangian approach. *Chem Eng Sci* 58: 5005–5024

Maier RS; Kroll DM; Kutsovsky YE; Davis HT; Bernard RS (1998) Simulation of flow through bead packs using the lattice Boltzmann method. *Phys Fluids* 10: 60–73

Moroni M; Cushman JH (2001) Statistical mechanics with three-dimensional particle tracking velocimetry experiments in the study of anomalous dispersion. II. Experiments. *Phys Fluids* 13: 81–91

Mueller, GE (1997) Numerical simulation of packed beds with monosized spheres in

- cylindrical containers. Powder Tech 92: 179–183
- Northrup MA; Kulp TJ; Angel SM; Pinder GF** (1993) Direct measurement of interstitial velocity field variations in a porous medium using fluorescent-particle image velocimetry. Chem Eng Sci 48: 13–21
- Ogawa K; Matsuka T; Hirai S; Okazaki K** (2001) Three-dimensional velocity measurement of complex interstitial flows through water-saturated porous media by the tagging method in the MRI technique. Meas Sci Technol 12: 172–180
- Peurrung LM; Rashidi M; Kulp TJ** (1995) Measurement of porous medium velocity fields and their volumetric averaging characteristics using particle tracking velocimetry. Chem Eng Sci 50: 2243–2253
- Rashidi M; Peurrung L; Tompson AFB; Kulp TJ** (1996) Experimental analysis of pore-scale flow and transport in porous media. Adv Water Resour 19: 163–180
- Ren X; Stapf S; Blümich B** (2005) Magnetic resonance visualization of flow and pore structure in packed beds with low aspect ratio. Chem Eng Tech 28: 219–225.
- Saleh S; Thovert JF; Adler PM** (1992) Measurement of two-dimensional velocity fields in porous media by particle image displacement velocimetry. Exp Fluids 12: 210–212
- Sederman AJ; Johns ML; Bramley AS; Alexander P; Gladden LF** (1997) Magnetic resonance imaging of liquid flow and pore structure within packed beds. Chem Eng Sci 52: 2239–2250
- Sederman AJ; Johns ML; Alexander P; Gladden LF** (1998) Structure-flow correlations in packed beds. Chem Eng Sci 53: 2117–2128
- Smereka P** (2006) The numerical approximation of a delta function with application to level set methods. J Comput Phys 211: 77–90
- Spinewine B; Capart H; Larcher M; Zech Y** (2003) Three-dimensional Voronoï imaging methods for the measurement of near-wall particulate flows. Exp Fluids 34: 227–241
- Stephenson JL; Stewart WE** (1986) Optical measurements of porosity and fluid motion in

packed beds. *Chem Eng Sci* 41: 2161–2170

Suekane T; Yokouchi Y; Hirai S (2003) Inertial flow structures in a simple-packed bed of spheres. *AIChE Journal* 49: 10–17

Tang C; Blatter DD; Parker DL (1993) Accuracy of phase-contrast flow measurements in the presence of partial-volume effects. *J Magn Reson Imag* 3: 377-385

Teng CL (2003) Interactions of rigid particles and liquid in a concentrated dispersion: Lagrangian computations and stereo imaging of RIM fluidisation experiments. Master Thesis, Department of Civil Engineering, National Taiwan University, Taipei, Taiwan

Tsorng SJ; Capart H; Lai JS; Young DL (2006) Three-dimensional tracking of the long time trajectories of suspended particles in a lid-driven cavity flow. *Exp Fluids* 40: 314–328

Yarlagadda AP; Yoganathan AP (1989) Experimental studies of model porous media fluid dynamics. *Exp Fluids* 8: 59–71

Zachos A; Kaiser M; Merzkirch W (1996) PIV measurements in multiphase flow with nominally high concentration of the solid phase. *Exp Fluids* 20: 229–231

Figure legends

Fig. 1. Schematic of the experimental set-up: **a** overview of the flow cell; **b** close-up of the measurement volume

Fig. 2. Photograph of the experimental set-up, showing the laser light sheet lens fed by an optical fibre link, to the left, and the CCD camera in the foreground of the flow cell

Fig. 3. Illumination and imaging configuration: **a** horizontal laser light sheet scanned at constant vertical speed used for the three-dimensional geometry measurements; **b** fixed vertical light sheet used for velocimetry measurements. The resulting laser-illuminated slices are viewed by the camera under the same oblique viewpoint

Fig. 4. Geometrical scan: **a** raw image sequence as acquired during the scan; **b** volumetric voxel image constructed by rectifying and stacking the raw image frames

Fig. 5. Sphere capture method illustrated on a two-dimensional analogue: **a** synthetic image composed of a set of circular halos; **b** pixel mask representing a discrete ring; **c** transformed image obtained by convoluting image **a** with mask **b**; **d** captured circles obtained by locating the intensity peaks of transformed image **c**

Fig. 6. Sphere capture method applied to the volumetric image obtained by laser scan: **a** cut-away through the voxel image; **b** cut-away through the transformed voxel image generated by convoluting volumetric image **a** with a voxel mask representing a discrete spherical shell; **c** spatial arrangement of the spheres obtained by locating the intensity peaks of transformed voxel image **b**

Fig. 7. Particle tracking velocimetry applied to laser-illuminated centre-plane: **a** close-up of background-subtracted colorized multiple exposure (with distinct gray levels representing blue-red-green-blue particle tracks); **b** close-up of micro-particle positions retrieved from four successive frames (each circle-square-triangle-diamond sequence represents a blue-red-green-blue track), with red-green particles paired manually using mouse clicks; **c** close-up of velocity vectors and sphere halos transformed back to spatial coordinates

Fig. 8. Procedure used to refine the spatial correspondence between the velocimetry and geometry data: **a** possible sphere positions with respect to the velocimetric laser plane, ambiguous as to whether spheres are to the front or back of the plane, **b** velocimetric plane halos (thick circles) and plane cross-section through the laser-scanned geometric packing of spheres (thin circles) before adjustment; **c** halos and cross-sections after optimal translation, and, **d** after optimal rotation adjustments of the velocimetric laser plane

Fig. 9. Observation and measurement results for the sphere packing geometry: **a** long exposure oblique view constructed from 50 frames of the scanning sequence; **b** vertically-averaged distribution of porosity over the tube cross-section

Fig. 10. Observation and measurement results for $Re = 28$: **a** long exposure image of the velocimetric plane resampled in spatial coordinates; **b** two-dimensional velocity field plotted jointly with the corresponding axial cross-section through the three-dimensional sphere packing. Square outlines indicate areas zoomed in for the close-ups shown at bottom; **c** close-up of the long exposure image; **d** close-up of the velocity field and sphere boundaries

Fig. 11. Transverse profiles across the flow cell: **a** radial profile of porosity obtained by averaging the porosity data of Fig. 9b along concentric annuli; **b** transverse profile of vertical velocity obtained by averaging over vertical bands the velocity field of Fig. 10b.

Fig. 12. Measured velocity distributions: **a** distribution of transverse velocity; **b** distribution of vertical velocity; **c** distribution of transverse velocity normalized by its standard deviation (dots), compared with the Gaussian normal distribution (line); **d** distribution of vertical velocity normalized by its mean value (black dots and lines). Our data ($Re = 28$) are compared with the data of Moroni and Cushman (2001) obtained at the Reynolds numbers $Re = 0.049$ (diamonds), 0.085 (squares), 0.105 (triangles) and 0.129 (circles)

Figures

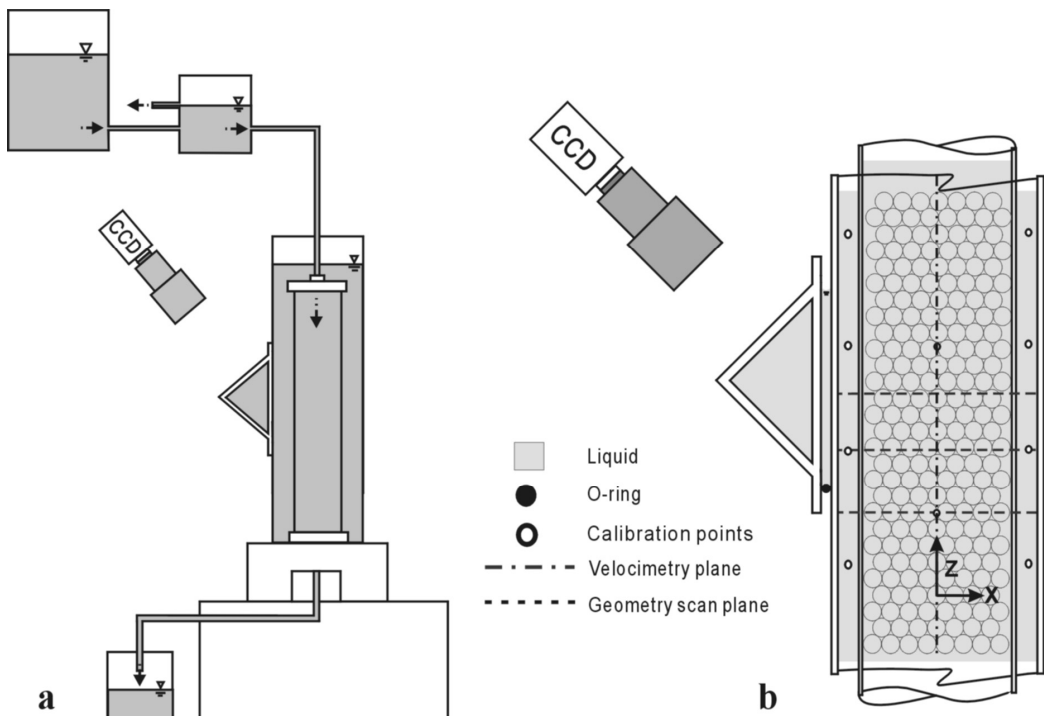


Figure 1

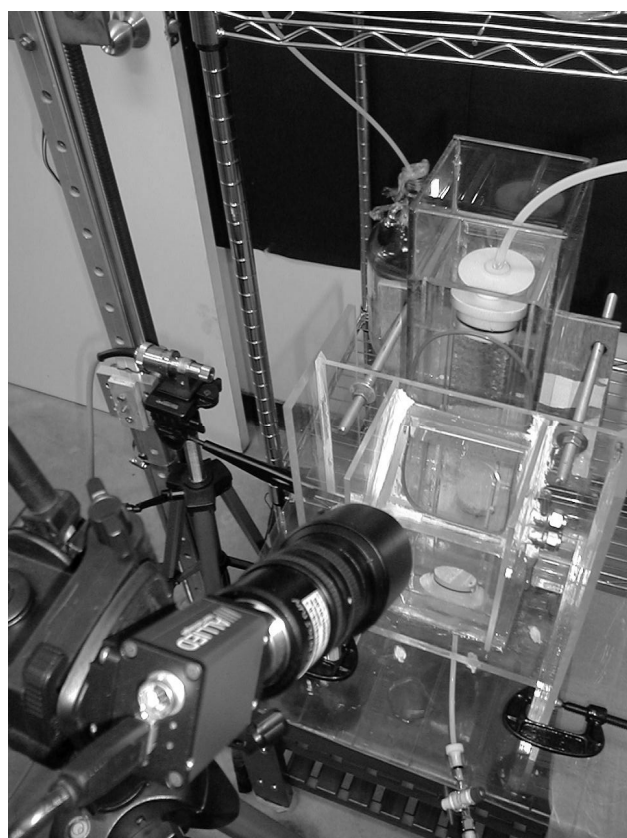


Figure 2

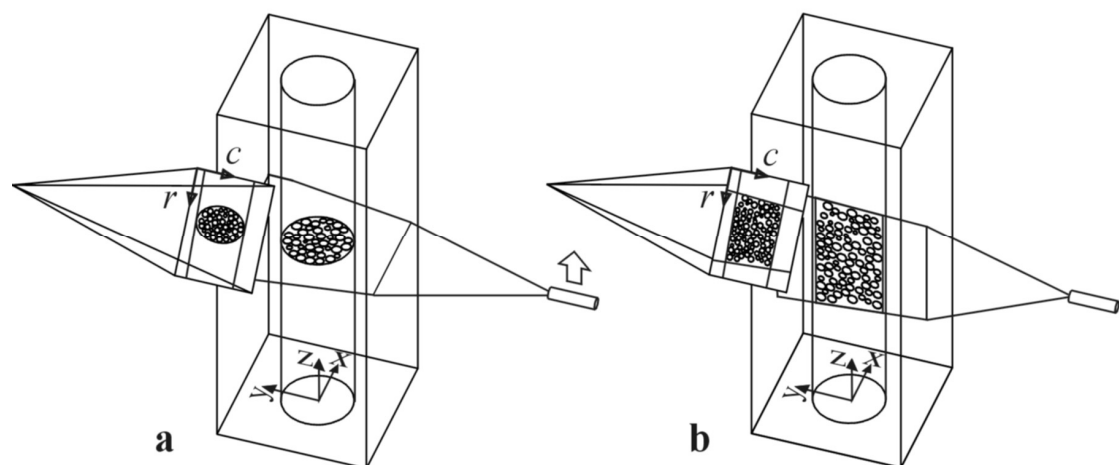


Figure 3

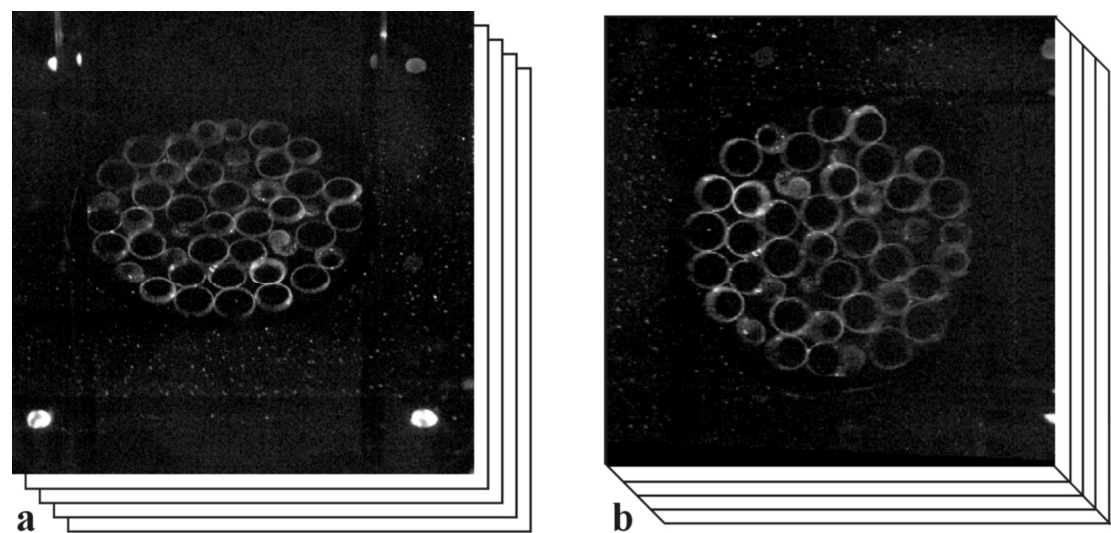


Figure 4

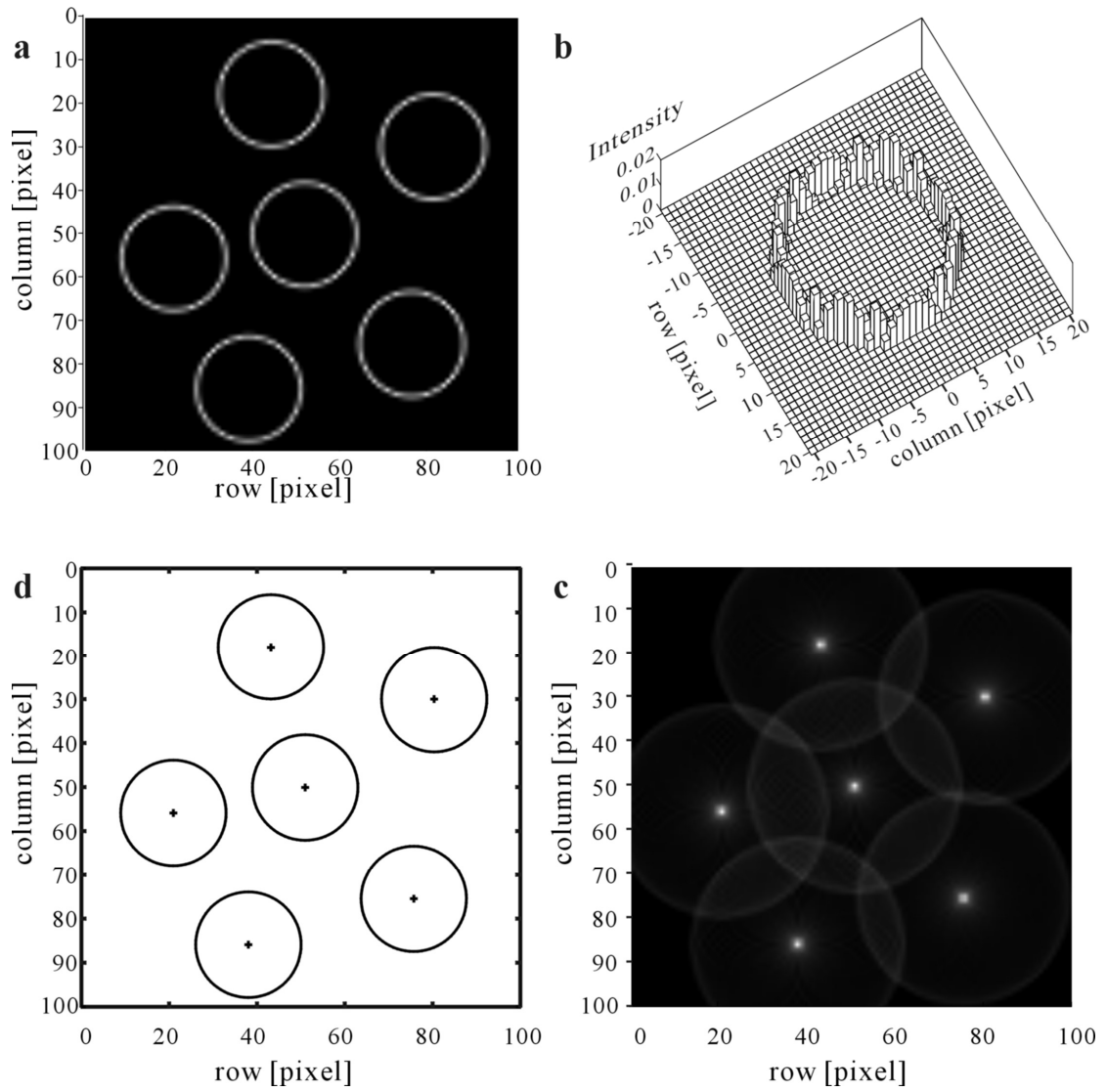


Figure 5

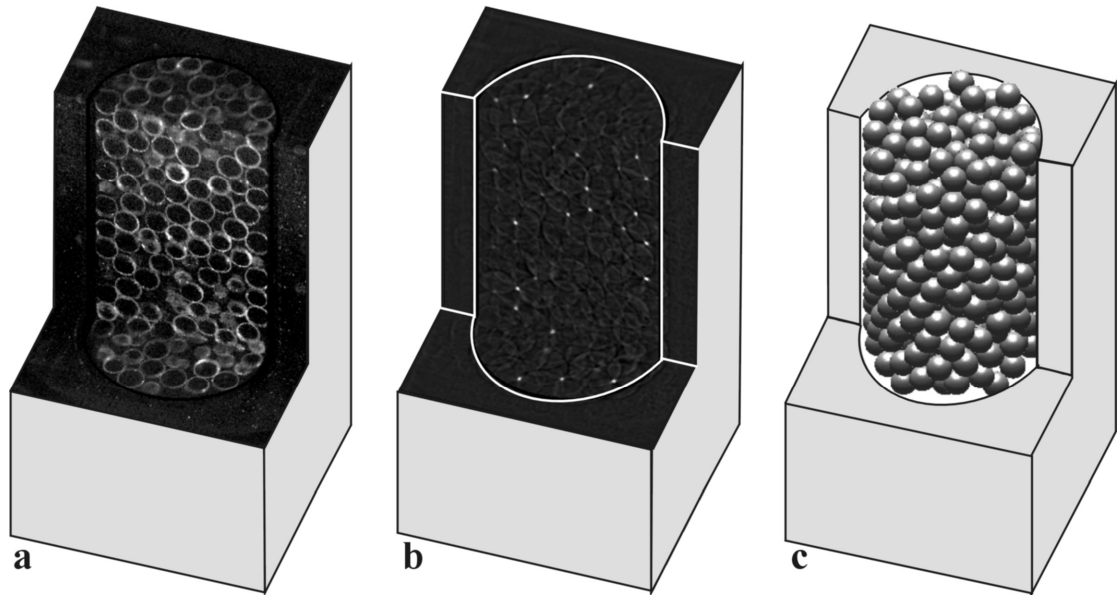


Figure 6

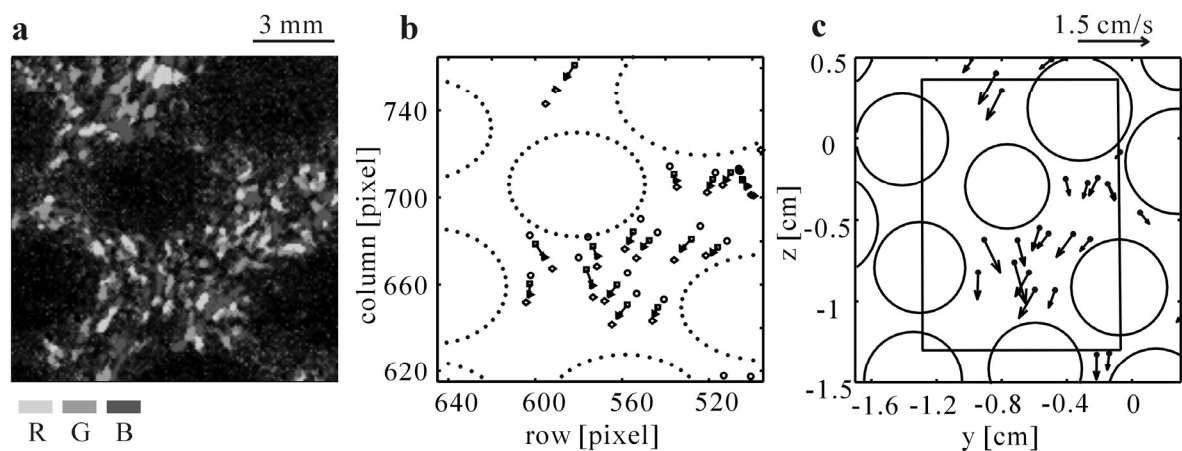


Figure 7

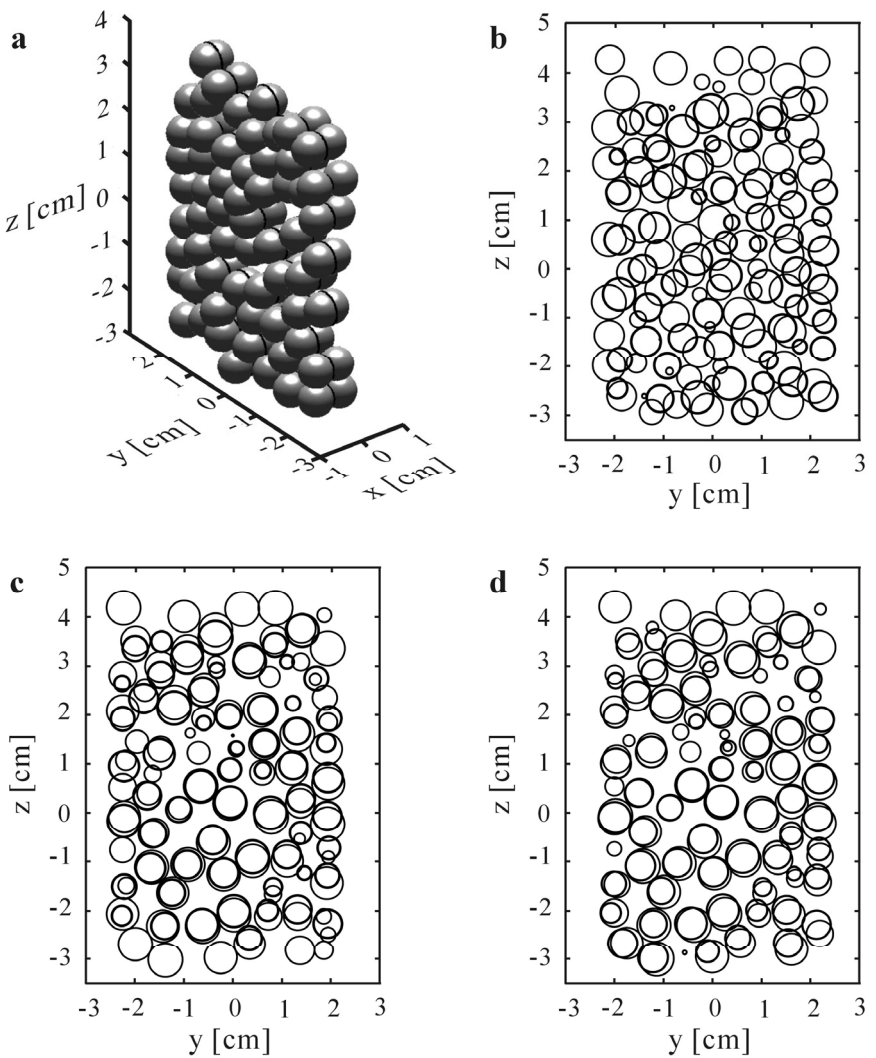


Figure 8

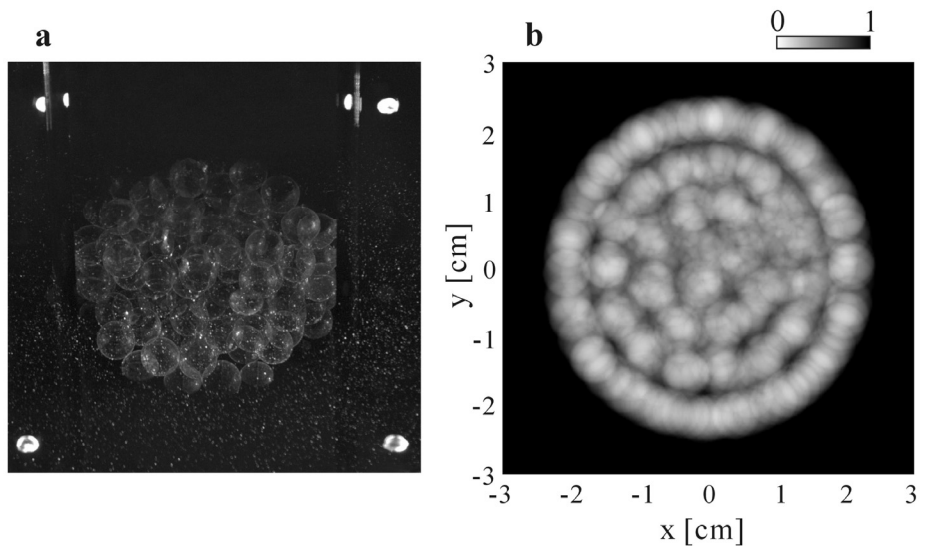


Figure 9

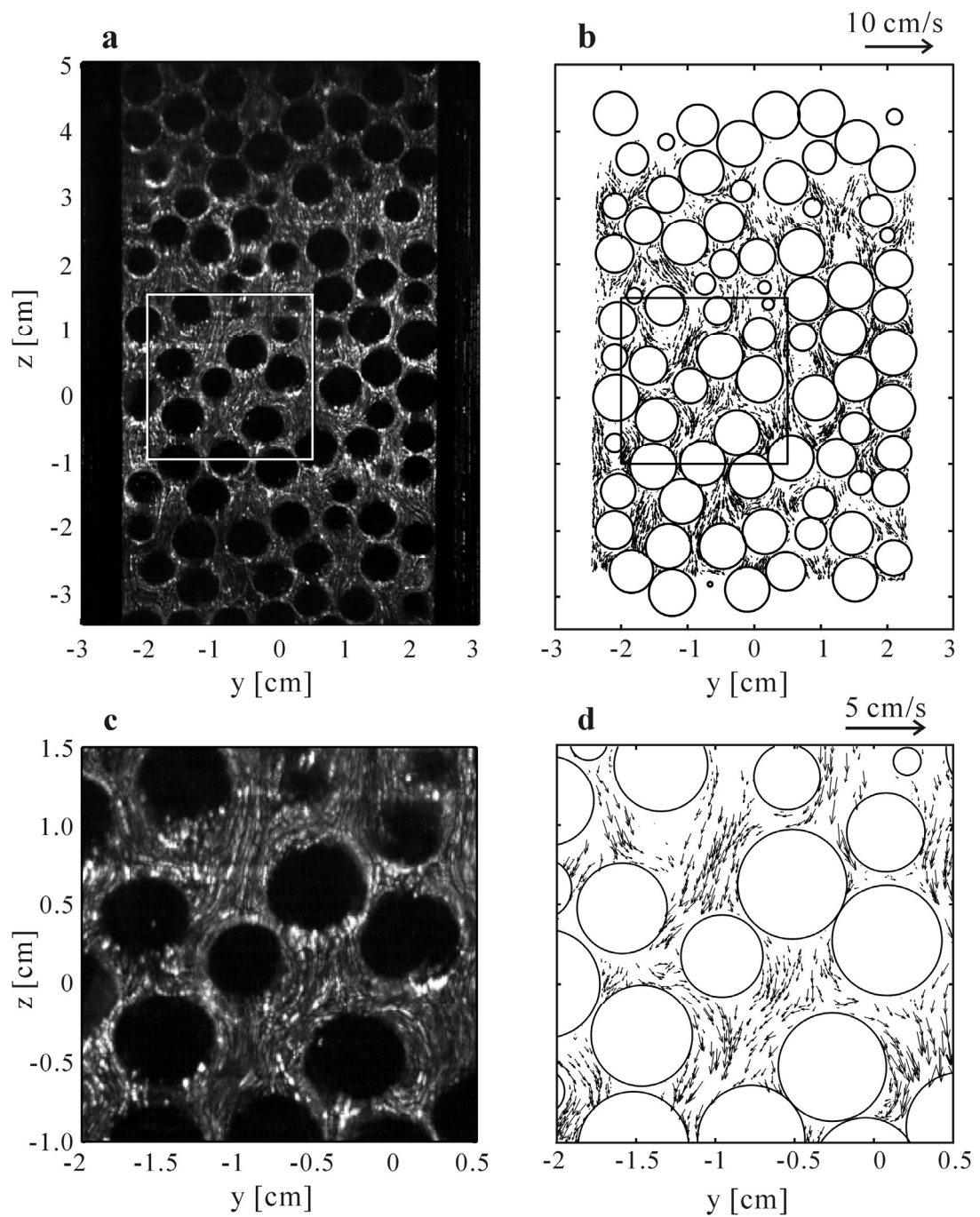


Figure 10

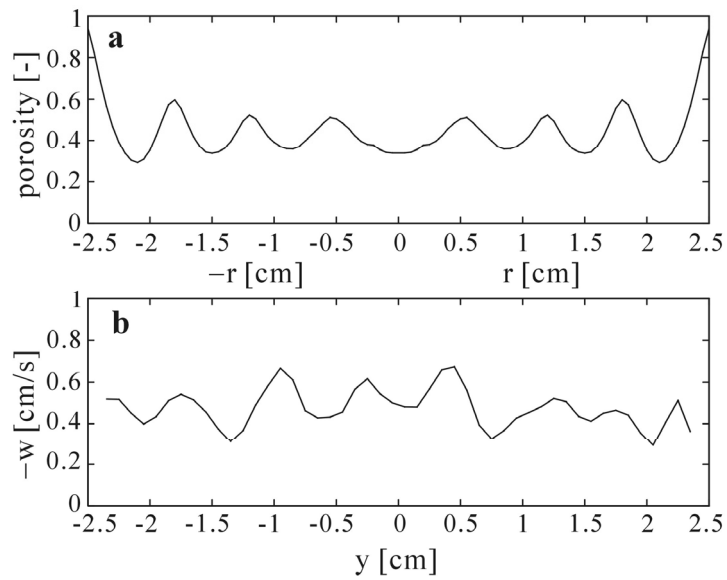


Figure 11

